NANO LETTERS
Letter
Cite This: Nano Lett. 2019, 19, 4620−4626
pubs.acs.org/NanoLett

Observation of Intersubband Polaritons in a Single Nanoantenna Using Nano-FTIR Spectroscopy

Chih-Feng Wang,[†,‡] Terefe G. Habteyes,[†] Ting Shan Luk,[§,∥] John F. Klem,[∥] Igal Brener,[§,∥] Hou-Tong Chen,[‡] and Oleg Mitrofanov*[,§,⊥]

[†]Center for High Technology Materials, University of New Mexico, Albuquerque, New Mexico 87106, United States
[‡]Center for Integrated Nanotechnologies, Los Alamos National Laboratory, Los Alamos, New Mexico 87545, United States
[§]Center for Integrated Nanotechnologies, Sandia National Laboratories, Albuquerque, New Mexico 87123, United States
[∥]Sandia National Laboratories, Albuquerque, New Mexico 87185, United States
[⊥]Electronic and Electrical Engineering, University College London, London WC1E 7JE, United Kingdom

Supporting Information

ABSTRACT: Strong coupling of an intersubband (ISB) electron transition in quantum wells to a subwavelength plasmonic nanoantenna can give rise to intriguing quantum phenomena, such as ISB polariton condensation, and enable practical devices including low threshold lasers. However, experimental observation of ISB polaritons in an isolated subwavelength system has not yet been reported. Here, we use scanning probe near-field microscopy and Fourier-transform infrared (FTIR) spectroscopy to detect formation of ISB polariton states in a single nanoantenna. We excite the nanoantenna by a broadband IR pulse and spectrally analyze evanescent fields on the nanoantenna surface. We observe the distinctive splitting of the nanoantenna resonance peak into two polariton modes and two π-phase steps corresponding to each of the modes. We map ISB polariton dispersion using a set of nanoantennae of different sizes. This nano-FTIR spectroscopy approach opens doors for investigations of ISB polariton physics in the single subwavelength nanoantenna regime.

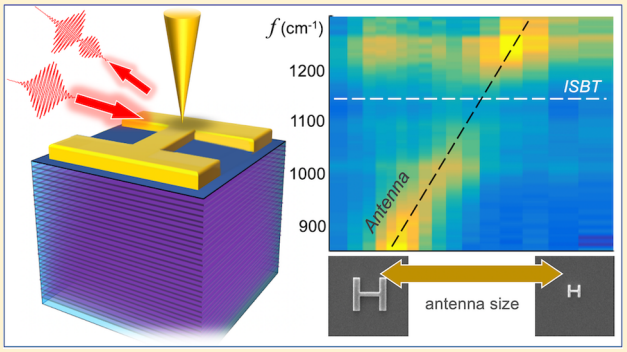

KEYWORDS: *Intersubband, polariton, near-field microscopy, quantum well, nanoantenna, nano-FTIR*

The electronic transition between the ground and the excited states in a doped semiconductor quantum well (QW), known as the intersubband (ISB) excitation,[1] is gaining more interest, because it enables a variety of devices, including quantum cascade lasers[2−4] and photodetectors,[5−7] across a wide range of wavelengths, from the far- to near-infrared (IR).[8] Intriguing quantum phenomena arise when the ISB electronic excitation forms a coherent superposition with the photon field, known as ISB polaritons,[9−12] which can be exploited in practical devices,[13] such as reconfigurable and nonlinear metasurfaces[14,15] and polariton light emitters.[16,17] An attractive property of ISB polaritons is their light−matter coupling strength, which is higher compared to interband polaritons (exciton−polariton) and which leads to the relatively unexplored regime of ultrastrong coupling.[18,19] Similar to polaritons involving other matter excitations, such as phonons and molecular and semiconductor excitons,[12] ISB polaritons have been predicted to display common polariton effects governed by quantum electrodynamics,[20,21] including boson behavior, polariton condensation, and polariton lasing with low threshold.[22] However, these effects, have not been reported yet for ISB polaritons, and theoretical frameworks[22,23] still require experimental verifications.

One of the challenges is that these effects require ISB polaritons confinement within a subwavelength volume, such as the mode of a nanoantenna, and it has been difficult to investigate ISB polaritons in a single nanoantenna experimentally. In fact, observation of ISB polaritons in the single nanoantenna regime has not yet been reported, whereas the smallest number of nanoantennae that produced a detectable signature of ISB polariton formation is 16.[24] Near-field microscopy however enabled direct investigation of nanoscale systems, including quantum dots,[25] nanowires[26] and monolayer materials,[27] as well as single nanoantennae.[28−32] The near-field approach was also exploited for spectroscopy of polaritons, albeit involving other matter excitations;[33−37] for example, the spatial distribution of phonon−polariton modes was observed in nanoantennae.[36,37] Here, we employ a scattering-type scanning near-field optical microscope (s-

Received: April 18, 2019
Revised: June 4, 2019
Published: June 10, 2019

DOI: 10.1021/acs.nanolett.9b01623
Nano Lett. 2019, 19, 4620−4626

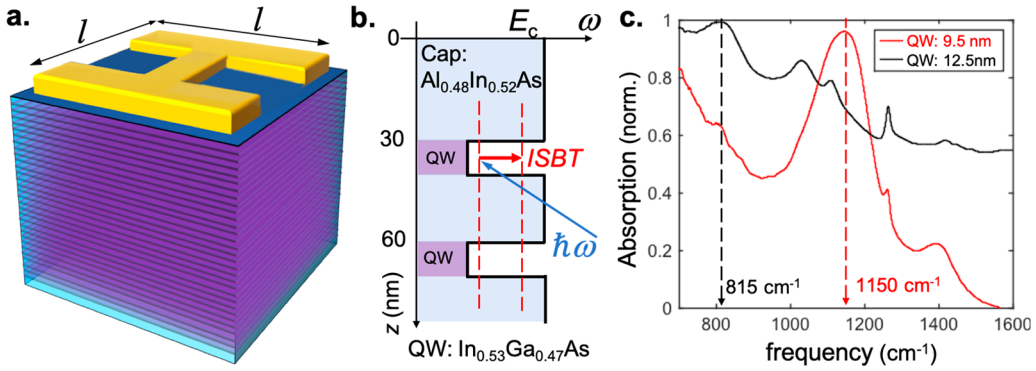

Figure 1. (a) Schematic of a dogbone nanoantenna above a QW stack. (b) Conduction band energy diagram showing two top $In_{0.53}Ga_{0.47}As$ QWs with $Al_{0.48}In_{0.52}As$ barriers (20 nm) and a 30 nm $Al_{0.48}In_{0.52}As$ cap layer; energy levels of the QW states are indicated by red dashed lines. (c) Experimental absorption spectra of two QW stacks revealing ISB absorption; the stacks contain 12.5 nm wide (black) and 9.5 nm wide (red) QWs. ISB absorption is calculated from experimentally measured transmitted light intensity for TM-/TE-polarized beams as $A = 1 - (T_{TM}/T_{TE})$.

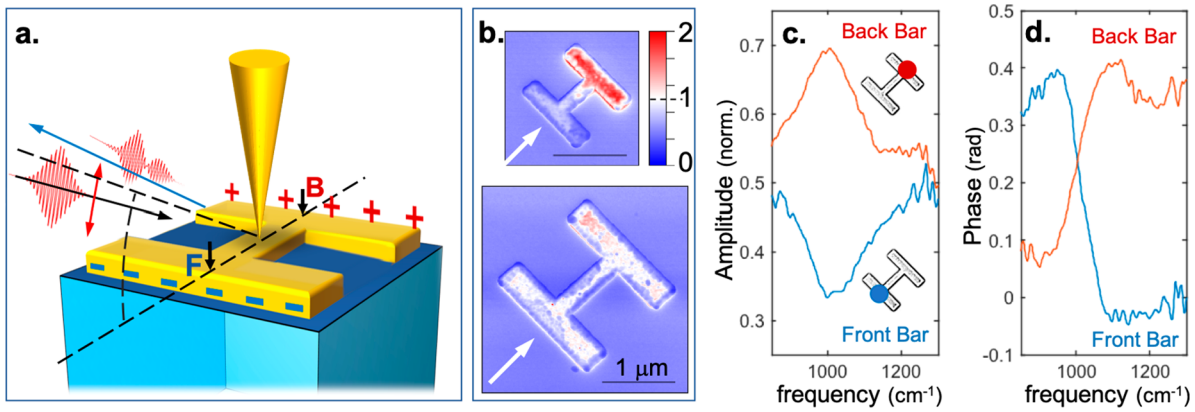

Figure 2. Near-field imaging and nano-FTIR spectroscopy of dogbone nanoantennae. (a) Schematic diagram of the experimental setup with black arrows marking the position of the s-SNOM probe on the front (F) and back (B) bars. (b) Near-field amplitude images (demodulated at 2Ω) for two nanoantennae illuminated at 1000 cm^{-1}: (top) nanoantenna in resonance with excitation (l = 950 nm) and (bottom) nanoantenna with the resonance below 1000 cm^{-1} (l = 1600 nm). In both images, the scale bars are 1 μm, and the scattered field amplitude is normalized to the average amplitude on the gold surface of the nonresonant (bottom) antenna. The white arrows indicate the propagation direction of the excitation beam. Nano-FTIR amplitude (c) and relative phase (d) for the l = 950 nm nanoantenna at the front/back (blue/red) bars; positions on the antenna surface where the spectra were taken are marked in insets in part c.

SNOM) to enable ISB polariton studies in the single nanoantenna regime, using nanoscale Fourier-transform infrared (nano-FTIR) spectroscopy. By analyzing evanescent fields on the surface of a nanoantenna fabricated on top of a stack of QWs, we detect splitting of the nanoantenna resonance into two polariton modes, upper and lower polaritons (UP and LP), indicative of strong coupling to the ISB transition in the QWs. Using nanoantennae of different sizes, we "tune" its dipolar resonance across the ISB transition and map the mode anticrossing. In addition to revealing the polariton energy splitting, the FTIR analysis of the evanescent fields allows us to measure the frequency-dependent phase for the two polariton modes. The nano-FTIR approach therefore opens doors to investigations of ISB polariton physics in the single nanoantenna regime, and it makes a step toward the goal of achieving the regime of a small number of excitations, in which the ISB polaritons were predicted to exhibit bosonic behavior and form a condensate.[22] Furthermore, direct measurement of the optical phase of the nanoantenna–ISB coupled system may aid in the development of practical applications, such as nonlinear ISB metasurfaces where engineering and controlling the local phase is essential for metasurface operation.

To enable investigations of ISB polaritons in the single nanoantenna regime, we first consider antenna geometry: first of all, it needs to satisfy the ISB transition selection rule and provide a strong optical field confined in a small volume to achieve the regime of strong coupling.[12] In the past, special microcavities were designed for observations of ISB polaritons.[9,10] However, subwavelength plasmonic resonators,[18,19,37,38] such as a dogbone-shaped nanoantenna, offered a better approach: metallic patches fabricated on the surface of a QW sample naturally provide (1) the required electric field component (perpendicular to QW plane) to satisfy the selection rule and (2) the resonant field enhancement in the subwavelength volume. Second, the nanoantenna geometry must be compatible with near-field probing. Although s-SNOM demonstrated remarkable capabilities for planar antenna probing,[28−33] application of s-SNOM for probing QW ISB polariton states has not yet been reported. The challenge for this surface sensitive technique lies in probing a nanoantenna mode, which is distributed below the surface, in the region of buried QWs. Recently, it was shown that a fraction of mode energy tends to leak to the top surface, even for modes with extremely strong subsurface confinement[30,39] suggesting that it is possible to probe ISB polaritons. As the

DOI: 10.1021/acs.nanolett.9b01623
Nano Lett. 2019, 19, 4620−4626

final consideration in selecting a nanoantenna geometry, we take into account the near-field probe interaction with the nanoantenna, which is known to produce spectral and spatial artifacts.[40,41] We will address the degree of interaction experimentally, and we will show later that for the selected nanoantenna geometry the interaction with the probe is negligible.

It was demonstrated previously that dogbone nanoantennae arranged in a planar array exhibit polariton formation when coupled to a stack of QWs.[38] Such a nanoantenna geometry produces enhanced fields underneath the surface with the electric field orientated perpendicular to the QW plane (Figure 1a) as required for ISB excitation (see the Supporting Information for numerical modeling). The antenna size l required for the dipolar resonance at 1000 cm^{-1} ($\lambda = 10\ \mu m$) is approximately 1 μm, and the corresponding mode is distributed within a depth of $\sim 0.5l$,[38] sufficiently deep to interact with a stack of ~20 QWs.

For the ISB system, we select doped $In_{0.53}Ga_{0.47}As$ QWs separated by $Al_{0.48}In_{0.52}As$ barriers. Schematics of the QW potential profile are shown in Figure 1b (see the Methods section for QW design details and the Supporting Information for band structure and electron wave function calculations). We use ~650 nm thick QW stacks, so that the nanoantenna mode is distributed entirely within the QWs to increase the interaction of the mode with the ISB transition. The width of the QWs allows us to "tune" the ISB transition energy. We use the width of 9.5 and 12.5 nm: one with the experimentally determined ISB transition at 1150 cm^{-1}, aligned with the center frequency of our IR pulse source (covering 850−1300 cm^{-1}), and the other at 815 cm^{-1}, below the pulse photon energy (Figure 1c).

To access the evanescent fields on the nanoantenna surface, we use two commercial s-SNOM systems (neaSpec GmbH), one equipped with a CW quantum cascade laser (QCL) (Daylight Solutions) tuned to 1000 cm^{-1}, and the other with a difference-frequency pulsed IR source and an FTIR spectrometer (see the Methods section for details). We excite the nanoantenna by a vertically polarized (TM-polarized) focused IR beam at 60° relative to the surface normal (Figure 2a), with the nanoantenna axis oriented in the plane of incidence. We bring a metal-coated AFM cantilever probe (Arrow NCPt, NanoWorld) to the antenna surface. The probe is driven to oscillate near its resonance frequency ($\Omega \sim 270$ kHz) with an amplitude of ~60 nm, and it scatters a small fraction of the evanescent field from the nanoantenna into far-field propagating waves. The scattered waves are collected with a parabolic mirror, and we extract the near-field contribution from the total scattered waves by demodulating the detected waves at higher harmonics.

To ensure that the demodulated signal carries information about nanoantenna excitation, we first investigate the spatial distribution of the scattered field using the CW QCL excitation and the pseudo-heterodyne detection method.[42] We select a nanoantenna of size l = 950 nm; this antenna is in resonance with the QCL radiation frequency (1000 cm^{-1}), and we map the scattered field amplitude over the antenna surface (Figure 2b, top). To avoid ISB excitation, we use the 12.5 nm QW stack in these experiments, so that the ISB transition (815 cm^{-1}) is not in resonance with the IR photons. Then, we record a scattered amplitude map for a larger nanoantennae, with the dipolar mode at a lower frequency (l = 1600 nm). For the l = 1600 nm antenna, we observe a uniform scattered field level over the entire nanoantenna surface (Figure 2b, bottom). In contrast, the resonant nanoantenna (l = 950 nm) exhibits different field amplitudes at the opposite bars (Figure 2b, top), indicating excitation of the dipolar mode.[32] We therefore conclude that the s-SNOM map reflects properties of the dipolar mode, despite the fact that the mode is distributed primarily in the QW region (see the Supporting Information for details).

Next, we excite the l = 950 nm nanoantenna by broadband IR pulses with the spectrum centered near 1000 cm^{-1} and analyze the evanescent fields for two locations on the antenna surface. We combine the scattered beam with a reference IR pulse in a Michelson interferometer and record their cross-correlation interferogram, whose Fourier-transform gives us the amplitude and phase of the scattered field with spatial resolution defined by the AFM probe (~25 nm). We also record the amplitude and phase of the scattered field for a relatively large gold patch and use it for normalization of the near-field signals. Figure 2c shows normalized nano-FTIR amplitude spectra collected when the tip is positioned at the opposite bars of the antenna. For the bar facing the IR source (*Front*), the spectrum shows a broad dip at 1000 cm^{-1}. In contrast, the spectrum of the opposite bar (*Back*) shows a peak around the same frequency (Figure 2c). To understand these spectra, we provide the following intuitive picture that describes two main components of the scattered signal. The first component is the *scattered evanescent field of the tip*, which carries information about the dielectric function of the material in the vicinity of the tip, and here we will refer to it as the tip contribution E_0; the second component is the *antenna evanescent field* E_A scattered by the tip. Only the latter component carries information about the antenna resonance, whereas the first component carries information about the material underneath the tip, specifically, the dielectric function of the material. We can distinguish these components within the measured spectra using fundamental properties of the dipolar antenna fields. These fields are both frequency- and position-dependent: the nanoantenna field E_A displays opposite polarity (180° out of phase) at the nanoantenna front and the back bars near the resonance frequency. On the other hand, the tip contribution is frequency-independent anywhere on the gold antenna surface (within the bandwidth of the IR pulse).[43] A superposition of E_A with the tip component E_0 therefore produces either a resonance peak or a dip in the nano-FTIR spectrum, depending on the phase of E_A at the nanoantenna opposite bars. We indeed observe such spectral features in Figure 2c: the dip and the peak correspond to the resonant antenna fields, being in and out of phase with the tip contribution, E_0. In contrast, the larger antenna shows no peaks within the same spectral range; i.e., the spectrum displays only the tip contribution E_0 (see the Supporting Information). The amplitude of the antenna contribution in Figure 2c is sufficiently large, approximately 1/3 of the tip contribution, and therefore, it allows us to see the resonances of the antenna clearly above or below the E_0 level. We note that the tip contribution may be eliminated using TE-polarized excitation, which does not couple to the tip directly. However, due to the limitations of the experimental system, we could not realize such a cross-polarized configuration. Nevertheless, we find that the antenna contribution for the dogbone nanoantenna is sufficiently strong: ($|E_A| \sim |1/3E_0|$ at the resonance), and thus, nano-FTIR spectroscopy can be performed directly in the standard TM-polarized configuration. We also note that

DOI: 10.1021/acs.nanolett.9b01623
Nano Lett. 2019, 19, 4620−4626

the spectral features on front and the back bars show similar resonance frequencies, similar line widths and amplitudes. This indicates that the near-field probe interaction with the nanoantenna is weak;[40] i.e., the resonance properties of the nanoantenna are not altered significantly by the probe (see the Supporting Information for detailed analysis).

In addition to the field amplitude spectra, the nano-FTIR analysis provides phase spectra, which also display a distinctive resonance signature (Figure 2d): we observe steplike changes at the antenna resonance frequency. The steps are of opposite direction for the front and the back bars, consistent with the opposite polarities of the antenna field. We note that the phase of the field is expected to vary with frequency from 0 to π around the resonance; however, the phase steps in Figure 2d are only ~0.3 rad.

To explain this apparent quantitative discrepancy, we display the detected near-field signal S_2 in the complex (phasor) plane in Figure 3a. Here, we represent every Fourier component as a vector with the length equal to the field amplitude $|S_2|$ and its direction defined by the phase. We find that the Fourier components in the complex plane describe two circular traces, for the front and the back bars, and the two contributions to the near-field signal become clearer: the resonant antenna field contribution E_A is a rotating vector, which changes its direction and length with frequency near the nanoantenna resonance, whereas the frequency-independent tip contribution E_0 is a stationary vector. These contributions are illustrated explicitly in Figure 3a as a black vector (tip contribution E_0) and a red vector (nanoantenna contribution E_A). The latter makes a circular rotation as frequency sweeps across the resonance. In the course of this rotation, the phase of the red vector changes by π, and the amplitude increases from zero, peaks at the resonance, and returns to zero at high frequencies. Since the resonant fields at the front bar are π out of phase from the phase at the back bar, the corresponding phasors originate from the same point (E_0) but describe two different circles, shown as blue and red traces in Figure 3b. The phasor diagram helps explain the observed phase steps quantitatively: since the total detected field is a vector sum of E_0 and E_A, the detected phase exhibits a small step, despite the fact that the phase of E_A varies by π.

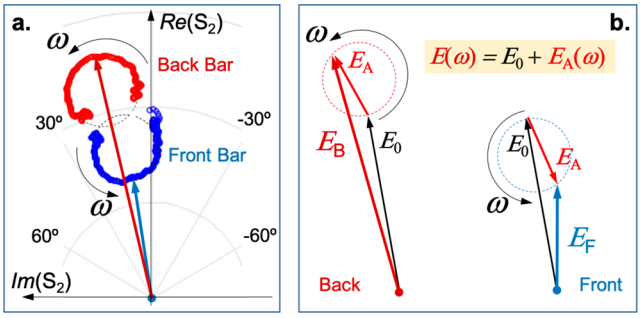

Figure 3. Nano-FTIR spectrum of the l = 950 nm dogbone nanoantenna represented in the complex (phasor) plane. (a) Fourier components (850−1268 cm^{-1}) plotted in the complex plane for the front/back (blue/red) bars. (b) Schematic phasor diagram for the scattered field illustrating superposition of the tip contribution (E_0) and the antenna contribution E_A (ω); the latter describes a circle as frequency increases.

Having identified the near-field signature of the nanoantenna resonance in the nano-FTIR amplitude and phase spectra, we now introduce coupling to the ISB excitation. To match the ISB transition at 1150 cm^{-1} to the nanoantenna dipolar resonance, we select an l = 850 nm nanoantenna and record nano-FTIR spectra for two identical nanoantennas fabricated on two samples with different QW designs. For the ISB at 815 cm^{-1}, the nanoantenna resonance is not coupled to the ISB transition, and the nano-FTIR spectrum shows a single resonance signature at ~1150 cm^{-1} (Figure 4a) consistent with the nano-FTIR results in Figure 2c,d. In contrast, the same nanoantenna design fabricated on the sample with the ISB transition at 1150 cm^{-1} shows two clear peaks in the amplitude spectrum, above and below the ISB transition energy, whereas the field enhancement at the resonance frequency of the uncoupled nanoantenna disappears entirely (Figure 4a). The splitting of the nanoantenna peak into two new peaks is similar to the far-field splitting of the ISB absorption band, and it indicates polariton formation.[38] The two polariton states show a distinctly different trace in the complex plane from the case of uncoupled nanoantenna (Figure 4c). The phasor describes a trace with two complete loops indicating that the corresponding phase changes by π for each of the two polariton states. We therefore conclude that ISB polariton formation in the single nanoantenna regime can be detected on the nanoantenna surface using s-SNOM. We also emphasize that not only the amplitude of the evanescent

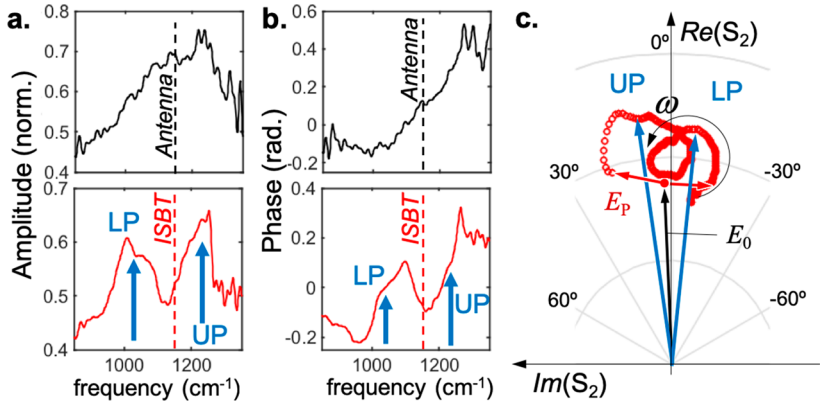

Figure 4. Nano-FTIR amplitude (a) and phase (b) spectra for the l = 850 nm nanoantenna with (red) and without (black) coupling to the ISB transition at 1150 cm^{-1} (vertical dashed lines). LP and UP frequencies are marked by blue arrows. (c) Fourier components (850−1268 cm^{-1}) of the near-field signal plotted in the complex plane.

DOI: 10.1021/acs.nanolett.9b01623
Nano Lett. 2019, 19, 4620−4626

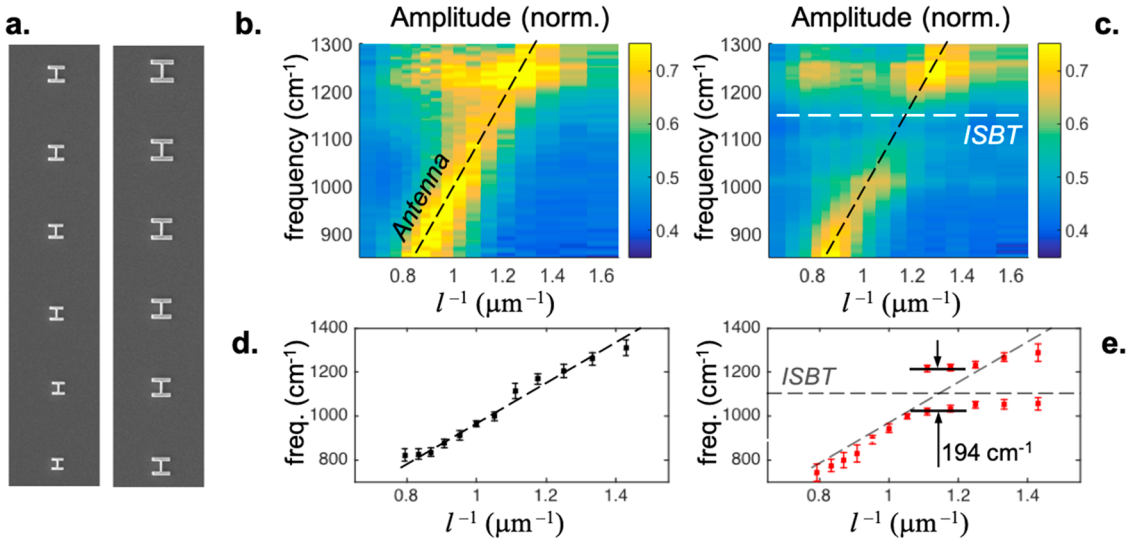

Figure 5. Nano-FTIR signature of nanoantennae with and without coupling to the ISB transition. (a) SEM images (4×23 μm^2) of 12 selected nanoantennae. (b) Scattered field amplitude map for the sample with the ISB transition (ISBT) at 815 cm^{-1} (outside the spectral range of the incident IR pulse). The nanoantenna resonance frequency is approximated by the black dashed line. (c) Scattered field amplitude map for the sample with the ISBT at 1150 cm^{-1} (marked by the white dashed line). Nanoantenna resonance frequencies (d) and ISB polariton frequencies (e) extracted from parts b and c, respectively, plotted as functions of the inverse antenna length.

field but also the phase is affected by the formation of the ISB polariton states.

We can now map dispersion characteristics of the nanoantenna−ISB system in the single nanoantenna regime. We fabricate a set of nanoantennae with size l ranging from 600 to 1600 nm (Figure 5a) and record amplitude and phase spectra at the same point on the back bar for every antenna. The results are shown as maps in Figure 5b,c, using the Fourier frequency and the inverse antenna length as coordinates (the corresponding phase maps are shown in the Supporting Information). For the 12.5 nm QWs the ISB transition is below the spectral range of IR excitation, and only the antenna resonance is present in the map: the amplitude peak shifts in frequency with the inverse antenna length practically linearly (Figure 5d). The same nanoantenna set fabricated on the 9.5 nm QW stack shows a similar behavior in the low- and the high-frequency ranges; however, in the region of the ISB transition, the nanoantenna resonance vanishes, and two peaks appear at 1030 and 1220 cm^{-1}, above and below the ISB mode, displaying the polariton anticrossing behavior. We note that both samples exhibit an increase in scattered amplitude at ~1250 cm^{-1}, close to the UP frequency; this increase can be also seen superimposed on the uncoupled nanoantenna and the UP peaks in Figure 4a. The increase occurs in the spectral region where our system exhibits additional absorption, and therefore the spectra are subject to additional noise. While it adds errors in determining the UP frequency, it does not obscure the nanoantenna peak splitting. We extract LP and UP frequencies from each antenna spectrum by fitting a sum of two symmetric functions (Gaussian line-shape) and a baseline to each nanoantenna spectrum. The LP and UP frequencies are shown in Figure 5e on top of the dispersion line for the uncoupled nanoantenna. We find that the polariton splitting at the frequency of nanoantenna resonance is ~194 cm^{-1}. It corresponds to the Rabi frequency ratio of 0.17, and therefore indicates the strong-coupling regime.

In summary, we demonstrate near-field spectroscopic analysis of ISB polaritons in the single plasmonic nanoantenna regime in the IR range (1150 cm^{-1}). By probing evanescent fields on the nanoantenna surface and performing FTIR spectroscopy, we observe splitting of the nanoantenna resonance into two polariton states as a result of strong light−matter coupling. The splitting manifests in enhanced amplitude of the evanescent field at frequencies above and below the nanoantenna resonance, as well as in the frequency-dependent phase, which we directly access using interferometric detection. This study demonstrates that s-SNOM can access ISB transitions in QWs by means of single plasmonic nanoantenna deposited on the sample surface. The nano-FTIR approach opens doors to a range of studies of ISB polaritons in the single nanoantenna regime, including investigations of the elusive effect of ISB polariton condensation. We anticipate that this near-field approach will also enable explorations of strong and ultrastrong light−matter coupling in the single nanoantenna regime for other excitations.[44,45] This approach also holds a great potential for probing nanoscale quantum systems not only positioned on the surface[25−27,35] but also buried within a depth of over 100 nm. For example, a small nonresonant nanoantenna may extend the reach of s-SNOM deeper below the surface and enable spectroscopy of ISB transitions in QWs without strong coupling. We also foresee that the possibility to detect the optical phase of nanoantenna−ISB polariton states will aid in the development of practical applications where knowledge of the local phase is essential, for example, for IR metasurfaces.

Methods. *Quantum Well Heterostructure Design and Fabrication.* The $In_{0.53}Ga_{0.47}As/Al_{0.48}In_{0.52}As$ heterostructure system is grown by molecular beam epitaxy (MBE) on a lattice matched InP substrate, with the QW width defining the ISB transition energy. We fabricated two QW stacks with different QW widths (9.5 and 12.5 nm). The QWs are separated by 20 nm thick $Al_{0.48}In_{0.52}As$ barriers, and the stacks are capped with a 30 nm thick $Al_{0.48}In_{0.52}As$ layer. The 9.5 nm QW stack contains 22 QWs, and the 12.5 nm QW stack contains 20 QWs; thus, the total thickness of the stacks is ~650 nm in both cases. The QWs are uniformly doped at the level of 1.25×10^{12}

DOI: 10.1021/acs.nanolett.9b01623
Nano Lett. 2019, 19, 4620−4626

cm^{-2} to have the ground QW level populated with electrons. Band structure and electron wave function calculations are provided in the Supporting Information. To determine ISB transition frequencies experimentally, transmission properties of both structures were tested using the waveguide configuration and a Fourier-transform infrared (FTIR) spectrometer. The ratio of the TM- to the TE-polarized light allows us to identify the energy of electron transition from the ground to the first excited state, i.e., the ISB transition frequency. The 9.5 nm QW sample displays an absorption peak at 1150 cm^{-1} and the 12.5 nm QW samples at 815 cm^{-1}. The bandwidth for both transitions is ∼100−150 cm^{-1}. The ISB transition frequency for the 9.5 nm QW samples is aligned with the photon energy of the IR pulses (∼850−1300 cm^{-1}), whereas the ISB transition energy for the 12.5 nm QW sample lies below it. We use the latter sample as a reference since it displays similar properties to the former sample except for the resonant ISB excitation.

Nanoantennae Design and Fabrication. We fabricate a nanoantenna using electron beam lithography (EBL) directly on the surface of the cap layer. Two layers of photoresist (PMMA495A4/PMMA950A4) are used to facilitate the lift-off process. After finding an optimal EBL dosage (450 $\mu C/cm^2$), antenna patterns are exposed in the photoresist and then developed in a solution of MIBK:IPA (1:3) for 60 s and rinsed in IPA for 20 s. We then deposit a 10 nm layer of titanium for adhesion followed by a 100 nm thick layer of gold using electron beam metal evaporation in vacuum. After the metal deposition, the photoresist is removed by soaking the samples in acetone. Identical antennae are fabricated on the surface of the two QW samples for comparison. All nanoantennae are described by the size parameter l (see the Supporting Information for design details). For l = 1000 nm, the width of the axial antenna bar is 125 nm, and the width of the side bars is 200 nm. This design is scaled proportionally to fabricate antennae with l ranging from 600 to 1600 nm, for which the expected resonance frequency ranges from 1800 to 700 cm^{-1}, respectively. All the antennae are fabricated on a relatively small sample area in a regular grid with a small spacing of 4 μm (Figure S1), to facilitate experimental near-field microscopy testing.

Near-Field Microscopy. We use a commercial AFM-based scattering-type scanning near-field optical microscope (neaSpec GmbH) and a commercial quantum cascade laser (QCL) (Daylight Solutions) operating in the CW regime at 1000 cm^{-1}. The illumination beam is polarized in the plane of incidence, and it is focused on the sample surface at an angle of 60° with respect to the surface normal using an off-axis parabolic mirror. A metal-coated AFM cantilever probe (Arrow NCPt, NanoWorld) was driven to oscillate with an amplitude of ∼60 nm. The backscattered wave is collected by the parabolic mirror, combined with a reference beam, and then focused on the IR detector.

Nano-FTIR Spectroscopy. A similar s-SNOM system (neaSpec GmbH) is used for spectroscopic analysis of the nanoantenna evanescent field. This s-SNOM system is coupled with an IR broadband pulse source (Toptica, FemtoFiber dichro mid-IR). To obtain nano-FTIR spectra the optical path of the reference arm of the Michelson interferometer is varied, and a corresponding interferogram is recorded. The total scanning length is 800 μm, resulting in spectral resolution of 6.4 cm^{-1}.

■ ASSOCIATED CONTENT

Supporting Information

The Supporting Information is available free of charge on the ACS Publications website at DOI: 10.1021/acs.nanolett.9b01623.

Details of the QW band structure and electronic states, SEM images, details of the near-field pseudo-heterodyne microscopy system and the nano-FTIR spectroscopy system, numerical modeling of nanoantenna resonance, analysis of near-field probe-nanoantenna coupling, and analysis of the nano-FTIR signatures of nanoantennae and ISB polariton splitting (PDF)

■ AUTHOR INFORMATION

Corresponding Author

*E-mail: o.mitrofanov@ucl.ac.uk.

ORCID

Chih-Feng Wang: 0000-0002-3085-6614
Terefe G. Habteyes: 0000-0001-5978-6464
Igal Brener: 0000-0002-2139-5182
Hou-Tong Chen: 0000-0003-2014-7571
Oleg Mitrofanov: 0000-0003-3510-2675

Author Contributions

I.B., H.-T.C., T.G.H., and O.M. conceived the idea and methodology. C.-F.W. performed nano-FTIR and near-field imaging studies and simulated nanoantenna properties. J.F.K. grew QW samples, and O.M. fabricated the nanoantenna samples. T.S.L. and O.M. performed far-field FTIR nanoantenna characterization in arrays. O.M. and C.-F.W. analyzed the experimental data and prepared illustrations. All authors contributed to the discussion of the results and to the editing of the manuscript. O.M. coordinated the overall research.

Notes

The authors declare no competing financial interest.

■ ACKNOWLEDGMENTS

We thank Dr. A. Benz for preliminary investigations, Dr. M. Goldflam for useful discussions, and Dr. Sebastian Gies for QW band structure modelling. This work was supported by the U.S. Department of Energy, Office of Basic Energy Sciences, Division of Materials Sciences and Engineering. Fabrication and nano-FTIR measurements were performed at the Center for Integrated Nanotechnologies, an Office of Science User Facility operated for the U.S. Department of Energy (DOE) Office of Science. Sandia National Laboratories is a multimission laboratory managed and operated by National Technology and Engineering Solutions of Sandia, LLC., a wholly owned subsidiary of Honeywell International, Inc., for the U.S. Department of Energy's National Nuclear Security Administration under contract DE-NA-0003525. Los Alamos National Laboratory, an affirmative action equal opportunity employer, is managed by Triad National Security, LLC for the U.S. Department of Energy's NNSA, under contract 89233218CNA000001. This article describes objective technical results and analysis. The views expressed in the article do not necessarily represent the views of the U.S. DOE or the United States Government. C.-F.W. and T.G.H. were supported in part by the U.S. National Science Foundation (Grant 1651478).

DOI: 10.1021/acs.nanolett.9b01623
Nano Lett. 2019, 19, 4620−4626

REFERENCES

(1) West, L. C.; Eglash, S. J. *Appl. Phys. Lett.* **1985**, *46*, 1156−1158.
(2) Faist, J.; Capasso, F.; Sivco, D. L.; Sirtori, C.; Hutchinson, A. L.; Cho, A. Y. *Science* **1994**, *264*, 553−556.
(3) Williams, B. S. *Nat. Photonics* **2007**, *1*, 517−525.
(4) Yao, Y.; Hoffman, A. J.; Gmachl, C. F. *Nat. Photonics* **2012**, *6* (7), 432.
(5) Levine, B. F. *J. Appl. Phys.* **1993**, *74*, R1.
(6) Nga Chen, Y.; Todorov, Y.; Askenazi, B.; Vasanelli, A.; Biasiol, G.; Colombelli, R.; Sirtori, C. *Appl. Phys. Lett.* **2014**, *104*, 031113.
(7) Palaferri, D.; Todorov, Y.; Bigioli, A.; Mottaghizadeh, A.; Gacemi, D.; Calabrese, A.; Vasanelli, A.; Li, L.; Davies, A. G.; Linfield, E. H.; et al. *Nature* **2018**, *556*, 85−88.
(8) Benz, A.; Campione, S.; Moseley, M. W.; Wierer, J. J., Jr; Allerman, A. A.; Wendt, J. R.; Brener, I. *ACS Photonics* **2014**, *1*, 906−911.
(9) Dini, D.; Köhler, R.; Tredicucci, A.; Biasiol, G.; Sorba, L. *Phys. Rev. Lett.* **2003**, *90*, 116401.
(10) Anappara, A. A.; De Liberato, S.; Tredicucci, A.; Ciuti, C.; Biasiol, G.; Sorba, L.; Beltram, F. *Phys. Rev. B: Condens. Matter Mater. Phys.* **2009**, *79*, 201303.
(11) Todorov, Y.; Sirtori, C. *Phys. Rev. B: Condens. Matter Mater. Phys.* **2012**, *85*, 045304.
(12) Frisk Kockum, A.; Miranowicz, A.; De Liberato, S.; Savasta, S.; Nori, F. *Nature Reviews Physics* **2019**, *1*, 19−40.
(13) Sanvitto, D.; Kéna-Cohen, S. *Nat. Mater.* **2016**, *15*, 1061−1073.
(14) Lee, J.; Tymchenko, M.; Argyropoulos, C.; Chen, P. Y.; Lu, F.; Demmerle, F.; Boehm, G.; Amann, M.-C.; Alù, A.; Belkin, M. A. *Nature* **2014**, *511*, 65−69.
(15) Lee, J.; Jung, S.; Chen, P. Y.; Lu, F.; Demmerle, F.; Boehm, G.; Amann, M. C.; Alù, A.; Belkin, M. A. *Adv. Opt. Mater.* **2014**, *2*, 1057−1063.
(16) Jouy, P.; Vasanelli, A.; Todorov, Y.; Sapienza, L.; Colombelli, R.; Gennser, U.; Sirtori, C. *Phys. Rev. B: Condens. Matter Mater. Phys.* **2010**, *82*, 045322.
(17) Geiser, M.; Scalari, G.; Castellano, F.; Beck, M.; Faist, J. *Appl. Phys. Lett.* **2012**, *101*, 141118.
(18) Todorov, Y.; Andrews, A. M.; Colombelli, R.; De Liberato, S.; Ciuti, C.; Klang, P.; Strasser, G.; Sirtori, C. *Phys. Rev. Lett.* **2010**, *105*, 196402.
(19) Geiser, M.; Castellano, F.; Scalari, G.; Beck, M.; Nevou, L.; Faist, J. *Phys. Rev. Lett.* **2012**, *108*, 106402.
(20) Ciuti, C.; Bastard, G.; Carusotto, I. *Phys. Rev. B: Condens. Matter Mater. Phys.* **2005**, *72*, 115303.
(21) Savasta, S.; Di Stefano, O.; Savona, V.; Langbein, W. *Phys. Rev. Lett.* **2005**, *94*, 246401.
(22) Colombelli, R.; Manceau, J.-M. *Phys. Rev. X* **2015**, *5*, 011031.
(23) Nespolo, J.; Carusotto, I. 2019, arXiv:1903.10213. arXiv.org e-Print archive. https://arxiv.org/abs/1903.10213.
(24) Malerba, M.; Ongarello, T.; Paulillo, B.; Manceau, J. M.; Beaudoin, G.; Sagnes, I.; De Angelis, F.; Colombelli, R. *Appl. Phys. Lett.* **2016**, *109*, 021111.
(25) Jacob, R.; Winnerl, S.; Fehrenbacher, M.; Bhattacharyya, J.; Schneider, H.; Wenzel, M. T.; von Ribbeck, H.-G.; Eng, L. M.; Atkinson, P.; Schmidt, O. G.; Helm, M. *Nano Lett.* **2012**, *12*, 4336−4340.
(26) Mooshammer, F.; Sandner, F.; Huber, M. A.; Zizlsperger, M.; Weigand, H.; Plankl, M.; Weyrich, C.; Lanius, M.; Kampmeier, J.; Mussler, G.; et al. *Nano Lett.* **2018**, *18*, 7515−7523.
(27) Schmidt, P.; Vialla, F.; Latini, S.; Massicotte, M.; Tielrooij, K.-J.; Mastel, S.; Navickaite, G.; Danovich, M.; Ruiz-Tijerina, D. A.; Yelgel, C.; et al. *Nat. Nanotechnol.* **2018**, *13*, 1035−1041.
(28) Neuman, T.; Alonso-González, P.; Garcia-Etxarri, A.; Schnell, M.; Hillenbrand, R.; Aizpurua, J. *Laser & Photonics Reviews* **2015**, *9*, 637−649.
(29) Bohn, B. J.; Schnell, M.; Kats, M. A.; Aieta, F.; Hillenbrand, R.; Capasso, F. *Nano Lett.* **2015**, *15*, 3851−3858.
(30) Deshpande, R.; Zenin, V. A.; Ding, F.; Mortensen, N. A.; Bozhevolnyi, S. I. *Nano Lett.* **2018**, *18*, 6265−6270.
(31) Habteyes, T. G. *J. Phys. Chem. C* **2014**, *118*, 9119−9127.
(32) Olmon, R. L.; Krenz, P. M.; Jones, A. C.; Boreman, G. D.; Raschke, M. B. *Opt. Express* **2008**, *16*, 20295−20305.
(33) Muller, E. A.; Pollard, B.; Bechtel, H. A.; Adato, R.; Etezadi, D.; Altug, H.; Raschke, M. B. *ACS Photonics* **2018**, *5*, 3594−3600.
(34) Park, K.-D.; May, M. A.; Leng, H.; Wang, J.; Kropp, J. A.; Gougousi, T.; Pelton, M.; Raschke, M. B. 2019, arXiv:1902.10314. arXiv.org e-Print archive. https://arxiv.org/abs/1902.10314.
(35) Wang, T.; Li, P.; Chigrin, D. N.; Giles, A. J.; Bezares, F. J.; Glembocki, O. J.; Caldwell, J. D.; Taubner, T. *ACS Photonics* **2017**, *4*, 1753−1760.
(36) Alfaro-Mozaz, F. J.; Alonso-González, P.; Vélez, S.; Dolado, I.; Autore, M.; Mastel, S.; Casanova, F.; Hueso, L. E.; Li, P.; Nikitin, A. Y.; Hillenbrand, R. *Nat. Commun.* **2017**, *8*, 15624.
(37) Jouy, P.; Vasanelli, A.; Todorov, Y.; Delteil, A.; Biasiol, G.; Sorba, L.; Sirtori, C. *Appl. Phys. Lett.* **2011**, *98*, 231114.
(38) Benz, A.; Campione, S.; Liu, S.; Montano, I.; Klem, J. F.; Allerman, A.; Wendt, J. R.; Sinclair, M. B.; Capolino, F.; Brener, I. *Nat. Commun.* **2013**, *4*, 2882.
(39) Mitrofanov, O.; Todorov, Y.; Gacemi, D.; Mottaghizadeh, A.; Sirtori, C.; Brener, I.; Reno, J. L. *Opt. Express* **2018**, *26*, 7437−7450.
(40) García-Etxarri, A.; Romero, I.; de Abajo, F. J. G.; Hillenbrand, R.; Aizpurua, J. *Phys. Rev. B: Condens. Matter Mater. Phys.* **2009**, *79*, 125439.
(41) Habteyes, T. G.; Dhuey, S.; Kiesow, K. I.; Vold, A. *Opt. Express* **2013**, *21*, 21607−21617.
(42) Ocelic, N.; Huber, A.; Hillenbrand, R. *Appl. Phys. Lett.* **2006**, *89*, 101124.
(43) Brehm, M.; Schliesser, A.; Cajko, F.; Tsukerman, I.; Keilmann, F. *Opt. Express* **2008**, *16*, 11203−11215.
(44) Yanagi, K.; Okada, R.; Ichinose, Y.; Yomogida, Y.; Katsutani, F.; Gao, W.; Kono, J. *Nat. Commun.* **2018**, *9*, 1121.
(45) Keller, J.; Scalari, G.; Cibella, S.; Maissen, C.; Appugliese, F.; Giovine, E.; Leoni, R.; Beck, M.; Faist, J. *Nano Lett.* **2017**, *17*, 7410−7415.

DOI: 10.1021/acs.nanolett.9b01623
Nano Lett. 2019, 19, 4620−4626